


METHODS ARTICLE OPEN ACCESS

Advantages and Limitations of Photoconvertible Probes to Study Subcellular Dynamics in Epithelial Cells

Mathieu Pinot^{1,2,3}  | Marie André⁴ | Chantal Roubinet^{1,2,3} | Céline Bruelle^{1,2,3} | Roland Le Borgne^{1,2,3} 

¹CNRS, UMR 6290, Rennes, France | ²Institut de Génétique et Développement de Rennes, Université Rennes, Rennes, France | ³Equipe Labellisée Ligue Nationale Contre le Cancer, Rennes, France | ⁴IGBMC (Institut de Génétique et de Biologie Moléculaire et cellulaire), Equipe Physique cellulaire, CNRS UMR 7104, Inserm U1258, Illkirch cedex, France

Correspondence: Mathieu Pinot (mathieu.pinot@univ-rennes.fr) | Roland Le Borgne (roland.leborgne@univ-rennes.fr)

Received: 18 July 2024 | **Revised:** 18 February 2025 | **Accepted:** 21 February 2025

Funding: MRic is member of the national infrastructure France-BioImaging supported by the French National Research Agency (ANR-10-INBS-04). Funding acquisition: R.L.B. (ANR-20-CE13-0015), M.P. (Université de Rennes, AAP défis émergents 2021).

Keywords: cellular imaging | diffusion | fluorescence techniques | light microscopy

ABSTRACT

The recent development of a wide variety of genetically encoded photoconvertible fluorescent proteins has made it possible to study unprecedented dynamic processes by monitoring sub-populations of cells or labeled proteins. The use of photoconvertible fluorescent proteins, such as Eos, KAEDE, mMaple3, Dendra2 is a major advance. However, the conditions of their use in vivo and the inherent potential side-effects remain poorly characterized. Here, we used *Drosophila* pupal notum to characterize in vivo the conditions for photoconversion (PC) at the subcellular level. We compared the ability to photoconvert proteins exhibiting distinct localization and dynamics, namely, cytosolic and transmembrane proteins fused to photoconvertible probes and expressed at physiological levels. We report that the restriction of PC to a predefined region of interest depends on the mobility of the tagged protein, the power of the PC laser and the number of iterations. We characterized the axial spreading inherent to one-photon microscopy, which results in a PC cone that limits probe tracking on the z-axis. We discussed how the use of a two-photon laser can overcome this issue. We detail biases in the use of photoconvertible probes and propose strategies to circumvent them. Overall, our study provides a framework to study protein behavior at the subcellular level in living organisms.

1 | Introduction

The recent advent of genome editing, combined with the development of fluorescent probes and advances in fluorescence imaging, have opened new avenues of research to study protein localization, dynamics, and interactions in cell cultures (Tsien 1998; Lippincott-Schwartz et al. 2001), as well as in complex 3D systems, such as organoids and model organisms (Rujano et al. 2022; Tomura et al. 2008; Lombardo et al. 2012). Approaches such as fluorescence resonance energy transfer/fluorescence lifetime imaging microscopy (FRET-FLIM) and fluorescence correlation spectroscopy (FCS), have led to major

improvements in determining, in addition to the localization, the interactions between two proteins independently of their diffusion rate. Although attractive, these two approaches may nonetheless require a dedicated microscopy setup (FCS) and a certain level of expertise, making them difficult to be used on a routine basis. Conversely, the most popular and accessible approach to determine proteins dynamical properties remains fluorescence recovery after photobleaching (FRAP) (Kang et al. 2010; Lippincott-Schwartz et al. 2001; Lippincott-Schwartz et al. 2018; Michelman-Ribeiro et al. 2009). This technique allows you to extract three parameters, the half-time recovery ($t_{1/2}$), the mobile (M), and the immobile fractions ($1-M$). The $t_{1/2}$

This is an open access article under the terms of the [Creative Commons Attribution-NonCommercial-NoDerivs](https://creativecommons.org/licenses/by-nc-nd/4.0/) License, which permits use and distribution in any medium, provided the original work is properly cited, the use is non-commercial and no modifications or adaptations are made.

© 2025 The Author(s). *Biology of the Cell* published by Wiley-VCH GmbH on behalf of Société Française des Microscopies and Société de Biologie Cellulaire de France.

provides information about the average mobility of the moving molecules, while M quantifies the fraction of moving molecules and $1-M$ describes the fraction of immobile molecules, such as those bound to proteins or lipids (Kang et al. 2010; Lele et al. 2004). FRAP, although easy to implement, is limited in that it can only measure diffusion coefficients of proteins in the photobleached region of interest (ROI). The development of photoactivatable probes, which modify their emission spectrum, makes it possible to monitor a specific population of labeled proteins in space and time inside as well as outside the ROI. In addition, photoconvertible fluorescent proteins enable the simultaneous study of the fate of photoconverted and non-photoconverted proteins (Ando et al. 2002; Mathur et al. 2012). Over the past decades, photoconvertible fluorescent proteins have commonly been used to track cells in zebrafish or mouse embryos (Lombardo et al. 2012; Hatta et al. 2006; Nowotschin and Hadjantonakis 2009) as well as to analyze the behavior of many proteins including the F-actin/ Myo II binding protein Supervillin (Fang et al. 2010), the chromatin marker Histone H2B, or alpha Tubulin, subunit of microtubules (Baker et al. 2010); (Leduc and Etienne-Manneville 2017). While cells were tracked within organisms, most of the subcellular protein monitoring was carried out in 2D cell cultures grown on glass coverslips. Recent studies on developing embryo of the sea urchin (Wavreil et al. 2021), *C. elegans* nervous system (Pigazzini and Kirstein 2020), *Drosophila* embryo (Wang et al. 2023), *Drosophila* neural stem cells (Roubinet et al. 2017) and *Drosophila* pupal notum (Trylinski et al. 2017) start to investigate proteins relocalizations at subcellular level within organisms with a temporal control. Moreover, some photoconversion (PC) protocols were established in zebrafish (Lombardo et al. 2012) and *C. elegans* (Hagedorn et al. 2013). However, they do not provide an exhaustive description of the limitations and the undesired spatiotemporal side effects inherent to this approach.

The first limitation in the use of photoconvertible probes is the temporal delay between the PC itself and the image acquisition in regards to the kinetic of diffusion of the tagged protein. A second limitation is the light illumination cone generated along the apical–basal axis by the laser beam, which hampers data interpretation of FRAP or PC (Bellec et al. 2021; Trylinski et al. 2017). Our methodological study provides a comprehensive description of the conditions used to perform green to red PC upon UV 405 nm illumination in vivo. We have used the *Drosophila* pupal notum and have compared the following parameters of UV 405 nm laser illumination: (i) laser power and number of iterations, (ii) the effects of the diffusion of the fluorescent photoconvertible proteins and (iii) the lateral location of the PC within the thickness of the tissue. To achieve this goal, we have made use of a variety of cytosolic and transmembrane proteins tagged with green to red photoconvertible probes. These probes include: Dendra2 derived from octocoral *Dendronephthya* sp. (Gurskaya et al. 2006; Baker et al. 2010), mMaple3 derived from the brown star *Clavularia* sp. (Wang, Moffitt et al. 2014), mEosFP derived from the coral *Lobophyllia hemprichii* (Wiedenmann et al. 2004) and KAEDE originating from the stony coral *Trachyphyllia geoffroyi* (Ando et al. 2002; Tomura et al. 2008). With the exception of KAEDE which was overexpressed, all other fluorescent probes are inserted at the locus, and hence results in functional reporters expressed at a physiological level. We report

that intrinsic properties of the proteins of interest coupled to the photoconvertible probes, such as their mobility, their time of residency at the plasma membrane and their localization along the apical basal axis must be taken into account when designing PC experiments. Furthermore, illumination parameters including laser intensity, number of iterations, must also be carefully considered. Our study provides a user guide for carrying out PC experiments on biological samples using confocal microscopes that are commonly found on imaging facilities in research institutes.

2 | Materials and Methods

2.1 | Key Resources

Key resources are listed in Tables S1 and S2.

2.2 | *Drosophila* Stocks and Genetics

All experiments were done according to ethical rules concerning the use of *Drosophila melanogaster*. Declaration of contained use of genetically modified organisms (GMOs) of containment class no. 2898 was made to the French Ministère de l'Enseignement Supérieur, de la Recherche et de l'Innovation. *D. melanogaster* stocks were maintained and crossed at 25°C. The stocks used in this study are listed in Table S1.

2.3 | Live Imaging

Live imaging was performed on pupae aged for 16–18 h after puparium formation (APF) at 22°C–25°C (Gho et al. 1999). Pupae were stuck on a glass slide with a double-sided tape and the pupal case were removed over the head and dorsal thorax using microdissection forceps. Spacers made with four to five glass coverslips were positioned at the anterior and posterior sides of the dissected pupae, respectively. A glass coverslip covered with a Voltalef 10S oil thin film was placed on top of the spacers. Images were acquired using the confocal mode of a LSM 880 Zeiss Airyscan microscope equipped with a 63x/1.4 NA Plan Apo objective and controlled by Zen black software. All images were processed and assembled using Fiji/ImageJ 1.54 and Adobe Illustrator.

For experiments using neural stem cells, 96 h after egg laying, larval brains were dissected in imaging medium and transferred onto a gas-permeable membrane (YSI Life Sciences 5793) fitted on a metallic slide. Brains were oriented with the brain lobes facing the coverslip. Excess media was removed until the brain lobes came into contact with the coverslip. The sample was sealed with Vaseline. Imaging medium (Schneider's insect medium (Sigma-Aldrich S0146) mixed with 10% FBS (Sigma), 2% PenStrep-Neo (Sigma), 0.02 mg/mL insulin (Sigma), 20 mM L-glutamine (Sigma), 0.04 mg/mL L-glutathione (Sigma) and 5 µg/mL 20-hydroxyecdysone (Sigma) was warmed up to room temperature before use.

2.4 | Photobleaching Experiments

Photobleaching of Dlg1::GFP and MyoII::GFP was performed using a Zeiss AiryScan (LSM 880 with AiryScan module) with the 488 nm laser wavelength (20 mW) at 100% of the maximal power and by using the 63× oil objective (NA 1.4). Two consecutive iterations were performed. The FRAP area was defined by orange dashed areas. A control area corresponding to an adjacent epidermal cell (EC) interface was measured to obtain the general photobleaching of the sample over the period of acquisition. All FRAP data were analyzed using the easyFRAP software tool (<https://easyfrap.vmnnet.upatras.gr/?AspxAutoDetectCookieSupport=1>). Half-time ($t_{1/2}$) and mobile fraction were then extracted with GraphPad Prism software using a one-component equation.

2.5 | PC Experiments

Photoconversion experiments were performed using a Zeiss Airyscan (LSM 880, Zeiss FRAP mode) equipped with a 405 nm diode (30 mW). The average pixel dwell time was set a 1.54 μ s according to previous PC assays using *Drosophila* nota (Trylinski et al., 2017; Bellec et al. 2021). UV 405 nm Laser diode power was set respectively at 0.5%, 1%, 2%, 5%, and 10%, that corresponds, respectively, to a power of 0.5, 2, 4, 11, and 22 μ W measured at 63X objective lens exit with a S121C Thorlabs standard photodiode Power Sensor. The number of iterations was defined between 1 and 40 depending on the fluorescent photoconvertible probes (Table 1 and Table S3). Photoconverted ROIs were drawn in dashed orange rectangles or discs. Two-photon PC was performed with a two-photon laser type Mai-Tai HP from Spectra Physics set to 810 nm at 0.5% (see Table S3 for associated power).

Apical and lateral PC assays were performed by making z-stacks (confocal sections of 0.5 μ m) before and after 405 nm (or 810 nm) PC. Before photoconversion, z-stacks were done to localize apical or lateral PC planes. After PC, z-stacks were directly acquired to observe the photoconverted apicobasal spreading.

For PC experiments in neural stem cells, 96 h larval brains expressing MyoII::Dendra2 were used. PC experiments were performed on an Andor Revolution spinning disc system according to (Roubinet et al. 2017). Several ROIs were manually chosen in the GFP channel and MyoII::Dendra2 was photoconverted with UV 405 nm just after anaphase onset.

2.6 | Analysis of PC Data

Analysis of PC experiments was performed using ImageJ v1.54. The quantifications of the amount of photoconverted signal (Figure 2E, Figure S3A,B, and Figure S5D) were obtained by subtracting the 561 nm signal before PC to the 561 nm channel intensities after PC. For PC assays presented in Figure 2 and Figure S5, the 561 and 488 nm channels relative fluorescence intensities of the photoconverted bicellular junction ROI were normalized by subtracting the respective cytoplasm background intensities. ROIs selection for quantifying the spatial spreading of the PC were manually selected as regions directly in contact with photoconverted ROI and corresponding (i) to the non-photoconverted part of the bicellular junction containing the

photoconverted ROI (Figure 2 and Figure S5) and (ii) to the entire non-photoconverted network of the cell containing the photoconverted MyoII network ROI (Figure 3 and Figure S3A,B). Statistical differences between the two conditions were evaluated by a Student's *t* test using GraphPad. Statistical significances were represented as follows: not significant (ns) *p* value ≥ 0.05 ; **p* value ≤ 0.05 ; ***p* value ≤ 0.01 ; ****p* value ≤ 0.001 .

2.7 | Measurement of the Light Cone

The theoretical angle was measured using the formula $NA = n \sin \theta$ where NA represents the numerical aperture of the 63X, which is 1.40, *n* the refractive index of oil of 1.518. The geometric angle of PC is measured using the formula $\tan \theta = \text{radius of the undesired photoconverted apical area} / \text{distance between the confocal plane of the photoconverted ROI and the confocal plane in which the unintended PC is observed}$.

3 | Results

3.1 | System Model and Fluorescent Photoconvertible Probe Selection

The *Drosophila* pupal notum is a monolayer epithelium of about 15 μ m in thickness and composed of two types of cells, ECs and sensory organ precursors (SOPs). The latter undergo asymmetric cell division and generate two daughter cells with different size and fate based on the differential activation of Notch signaling (Schweisguth 2015). The *Drosophila* genetic toolbox allows to perform efficient genome editing and dissect genetically the biological processes of interest. This system also enables noninvasive and quantitative live-imaging of functional fluorescently tagged proteins that are expressed at physiological levels and are functional. We chose probes to tag proteins that differ in FRAP recovery timescale, from seconds to hours, as well as on their steady-state localization in the cytoplasm, at the plasma membrane, at given cortical domains or cytoskeletal elements. We used cytosoluble KAEDE, which diffuses freely into the cytoplasm (3D diffusion, $M \sim 0.98 \pm 0.05$ and $t_{1/2} < 50$ ms (Bakshi et al. 2011; Table 1; Bruelle et al. 2023; Daniel et al. 2018), and GAP43 (GAP43::mEos), a growth-associated protein 43 which contains a dual palmitoylation signal that anchors the protein to the inner leaflet of the plasma membrane (Mavrikakis et al. 2009; Campbell et al. 2002). We also used components of septate junctions (SJ), which form a belt of 3 to 4 μ m thick. SJ markers include the cortical polarity protein Discs large 1 (Dlg1::Dendra2) which exhibits a rapid recovery, in the second time scale following photobleaching (3D diffusion, $M \sim 0.79 \pm 0.06$ and $t_{1/2}$ is 1.7 ± 0.5 min (Oshima & Fehon and 2011); $M \sim 0.85 \pm 0.07$ and $t_{1/2} \sim 19$ s obtained from our study Figure S6), and the transmembrane core-component Na⁺/K⁺ ATPase beta subunit Nervana2::Dendra2 (Nrv2::Dendra2), which has a slow mobility over a 60-min period in the embryo ectoderm and pupal notum (3D diffusion, $M \sim 0.38$ and $t_{1/2} \sim 6$ min (Oshima and Fehon 2011); $M \sim 0.19$ and $t_{1/2} \sim 45$ min for ATP-alpha obtained from (Daniel et al. 2018). We also used another transmembrane protein, the Notch receptor fused to mMaple3 or Dendra2 (Notch::mMaple3 Trylinski et al. 2017) or Notch::Dendra2 (Bellec et al. 2021). This probe exhibits a short residency time at the apical and

TABLE 1 | Summary tables of PC condition in function of the mobility of fluorescent proteins in the *Drosophila* pupal notum.

Protein localization			FRAP recovery parameters			Conditions			PC protocol				
	Protein of interest	Mobile fraction	t _{1/2}	[ref]	Power (%)	it	Problems	Recommendations	[ref]				
Cytosol	Free diffusion	0.98 ± 0.06	<< 50 ms	Bakshi 2011	1	1	Lateral diffusion within cell	High speed microscopy (spinning disc)	Figures S2 and S5				
	Acto-myosin cytoskeleton	0.92 ± 0.06	5.2 ± 1.8 s	Figure S6	2 5 10	2 2 2	Lateral diffusion outside ROI	Low laser power	Figure 3				
Plasma membrane	Cortical proteins	0.89 ± 0.09	8.8 ± 2.8 s	Figure S6	2	40	Lateral diffusion and photobleaching	Iterations decrease	Figure S2				
					10	30	Lateral diffusion and photobleaching	Iterations decrease	Figure S2				
	Septate junction Cytosolic Dlg1	0.85 ± 0.07	19.2 ± 6 s	Figure S6	2	40	Lateral diffusion outside ROI	Iterations decrease	Figure 2				
	Transmembrane proteins	Adherens junction Notch	0.31	36.8 ± 11 s	Bellec 2021	Ni::Dendra2	Not detected	Figures S1 and S2					
	Septate junction	< 10 mn 0.19	28 ± 6 s	Daniel 2017	2	40	Apicobasal spreading	Bi-photon PC but low efficiency & high PC duration	Figure 5 and				
	Core component ATPa/Nrv2	> 10 mn 0.8	45 mn						S5				

Note: Summary table of proposed photoconversion parameters for photoconvertible proteins depending on their localization, and their mobility (based on GFP-FRAP measurements). First and Second columns represent the fluorescent protein localization in the pupal notum of *D. melanogaster*. Third column represents the FRAP recovery parameters of GFP associated probes in the pupal notum (except for KAEDE (Bakshi et al. 2011). Fourth column represents the photoconversion laser power and iterations number tested in the present study associated to the encountered problems and advices. The laser power correspondence is presented on Table S3.

lateral plasma membrane of SOP daughter cells where it is proteolytically activated upon ligand binding (Houssin et al. 2021; Couturier et al. 2013; Bellec et al. 2021; Trylinski et al. 2017). Notch::GFP has a low diffusion coefficient with a mobile fraction $M \sim 0.30$ and $t_{1/2}$ around 38 s (Houssin et al. 2021). At last, we used the non-muscle Myosin II regulatory light chain fused to Dendra2 (MyoII::Dendra2), which is associated with the contractile actomyosin cytoskeleton. This probe is located apically in the plane of adherens junctions (AJs) (Heisenberg and Bellaïche 2013) and at the midbody during cytokinesis. Myosin II exhibits fast kinetics with a mobile fraction of around 0.9 ± 0.09 and a $t_{1/2}$ of around 5 s to 9 s depending on its localization on pupal notum (Table 1; Figure S6). Overall, and based on FRAP measurements, our study aims to investigate the conditions and effects of PC on probes with very different mobilities.

We first made sure that the addition of photoconvertible probes did not interfere with the subcellular localization of proteins, which was the case for all except Notch::Dendra2 (Figure S1A). When compared to Notch::GFP and Notch::mMaple3, Notch::Dendra2 is hardly detected at the plasma membrane (Figure S1B–B' and (Bellec et al. 2018; Houssin et al. 2021). We propose that Notch::Dendra2 present at the plasma membrane corresponds to the newly synthesized protein in which the Dendra2 moiety is not yet folded, hence not yet fluorescent (Bellec et al. 2021). The fact that the residence time of the full length Notch at the plasma membrane is in the minute time scale (Houssin et al. 2021) also contributes to the absence of detection of Notch::Dendra2 at the plasma membrane. Unlike Notch, Nervana2 has a high residence time and a low mobile fraction (Oshima and Fehon 2011), which accounts for Nrv2::Dendra2 being detected at the plasma membrane. These data suggest that the folding rate of the photoconvertible probe is relative to the kinetics of synthesis and half-life of the tagged may be a limiting factor when designing PC experiments.

3.2 | Applications of Photoconvertible Probes to Monitor Several Aspects of Cell Division in *Drosophila*

We next explored different experimental conditions for PC at different spatiotemporal resolutions in interphase and dividing epithelial cells. We have used cytosoluble KAEDE to monitor the timing of the physical separation of daughter cells during cytokinesis. We reported that KAEDE diffuses efficiently between daughter cells until the completion of abscission (Bruelle et al. 2023; Daniel et al. 2018). As KAEDE is freely diffusing within the cytosol, a single point pulse of laser (orange points, Figure S1C,C') at 405 nm is shown to be sufficient to recover photoconverted KAEDE in the entire cytosol of the targeted cell within 2 s (Figure S1C,C'). If cells have not yet undergone abscission, KAEDE is in a dynamic equilibrium between daughter cells (Figure S1C). In contrast, when daughter cells are physically separated, KAEDE remains restricted to the photoconverted cell (Figure S1C'). The PC and imaging setups used in the previous experiments are well suited to determine the timing of abscission (Bruelle et al. 2023; Daniel et al. 2018). However, they do not suffice to monitor the diffusion of soluble photoconverted probe in the cell volume. In this case, the imaging speed becomes the limiting factor, and requires a more sensitive device, such as spinning disc confocal

microscope capable of acquiring images at the millisecond scale (Woods et al. 2014).

In contrast to rapidly, freely-diffusing KAEDE at the millisecond time scale, probing cytoskeletal element post PC, such as MyoII, which exhibits FRAP recovery parameters with a $t_{1/2}$ of ~ 5 s to 8 s and a 0.9 mobile fraction, is achievable using classical scanning confocal microscope (Figure 1A,B). We monitored the behavior of the apical medial network of MyoII::Dendra2 in ECs and SOP cells (Figure 1B). Two s after PC of a $1.2 \mu\text{m}$ diameter disc ROI set in the middle of the apical MyoII network, the EC and SOP MyoII medial network are efficiently photoconverted. 60 s after PC, photoconverted MyoII is no longer restricted to the ROI but found at distance, at the junctional pool of MyoII, as expected for the actomyosin cytoskeleton (Figure 1B'; lower panel; black arrows). Nonetheless, 2 s after UV laser excitation, the photoconverted MyoII is also detected outside the selected ROI in a graded manner (Figure 1B'; white (upper panel) and black (lower panel) arrows). This may be because the temporal resolution of our current imaging setup is not fast enough. Thus, in 2 s, a part of the photoconverted signal has already diffused out of the ROI, as observed using KAEDE (Figure S1C). To test whether this is due to imaging limitations, we performed similar experiments using Nrv2::Dendra2, which exhibits slower mobility (Oshima and Fehon 2011); (Daniel et al. 2018). We photoconverted an ROI that comprised a portion of the plasma membrane of a SOP undergoing cytokinesis (Figure 1A,C). We observed that the photoconverted signal remained restricted to the ROI after the UV pulse (Figure 1C'; from t_2 s to t_{10} min). We also did similar experiments with the MyoII-positive midbody (Figure 1A,D), which results from constriction of the actomyosin ring at the end of cytokinesis (Daniel et al. 2018). The midbody is formed basally to the AJ (Daniel et al. 2018) and exhibits low FRAP recovery rate (Wang et al. 2019). PC is effective and remains restricted to the midbody in the confocal plane of the photoconverted ROI 2 s after PC (Figure 1D', bottom panel). However, we observed that the MyoII present apically at the AJ plane was also photoconverted (Figure 1C,C', upper panel, z-stack performed 30 s following midbody PC). This undesirable axial PC is a consequence of the geometry of the laser beam, that presents a double cone shape with a measured θ geometrical angle of about 60° (theoretical 67° , see Section 2) (Figure 5; Figure S5A).

Our experiments demonstrate that PC is restricted to the ROI within the plane of observation, arguing that the photoconverted medial MyoII::Dendra2 signal detected outside the ROI 2 s after the UV laser pulse (Figure 1B') is most likely due to the fast mobility of the photoconvertible fluorescent protein, a possibility that we explore next.

3.3 | Impact of the Diffusion Rate of Probes on Their Spatiotemporal Tracking Following PC

The above results indicate that a priori knowledge in the mobility of the protein of interest is informative to select PC parameters such as laser power and number of iterations. For all the experiments, we set the pixel dwell time at $1.54 \mu\text{s}$, as recommended in (Trylinski et al. 2017), and measured the laser power at 63X lens exit (Table 1 and Table S3). While a single iteration at 405 nm of a $0.5 \mu\text{m}^2$ ROI at 1% laser intensity (2

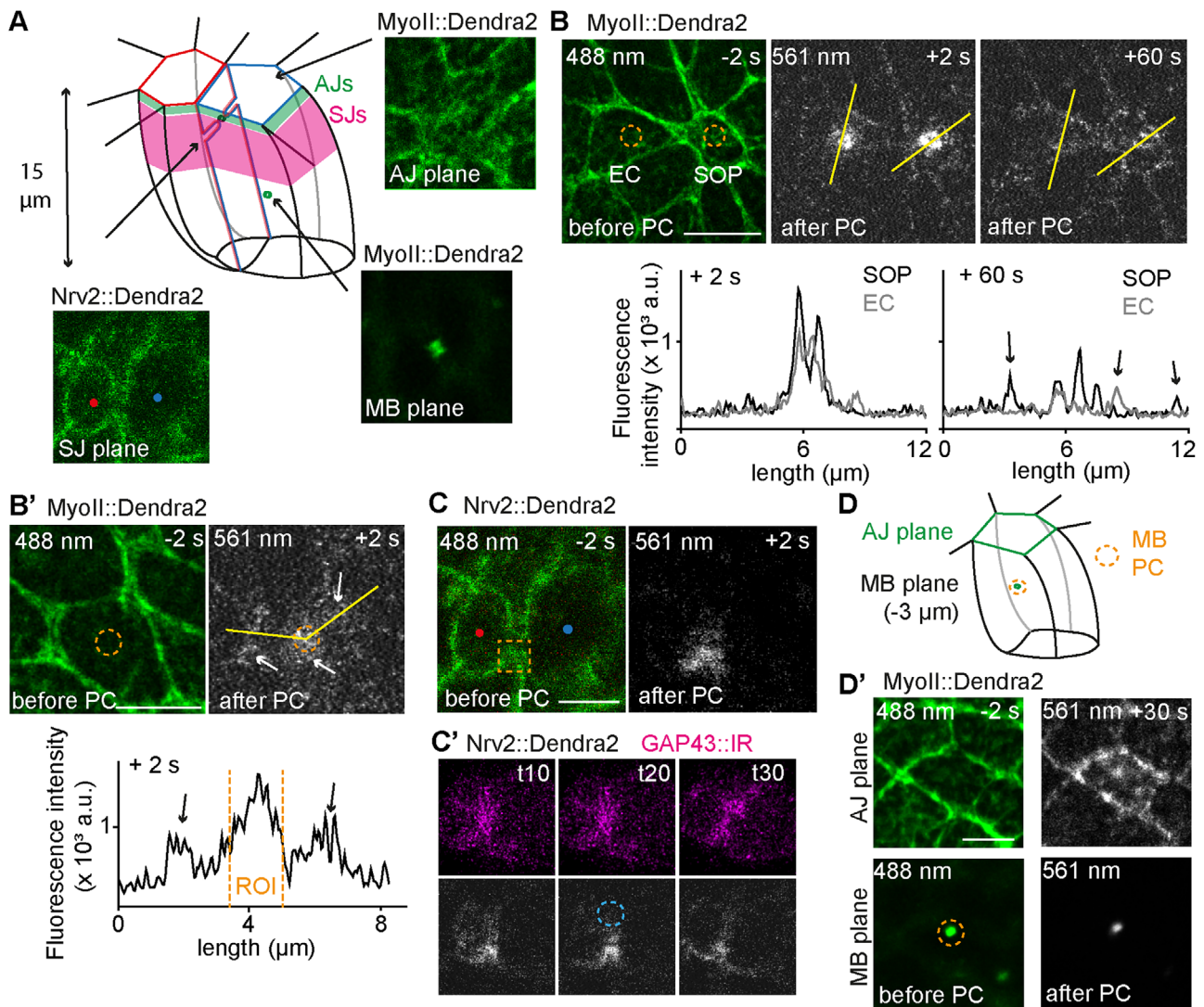


FIGURE 1 | Photoconvertible fluorescent proteins to monitor several aspects of cell division in *Drosophila*. (A–A') Schematic representation of the SOP daughter cells pIIb (red) and pIIa (blue) of the *Drosophila* pupal notum. Green rectangles represent the localization of PC experiments performed in (B–C–D). (A') Localization of the junctional and medial MyoII::Dendra2 in the plane of adherens junction (AJ) of SOP (i) and in the midbody at the pIIa-pIIb stage (iii), and localization of the SJ component Nrv2::Dendra2 at the pIIa-pIIb stage. (B) PC of the medial MyoII medial network in ECs and SOP cells. Plot profile of photoconverted (561 nm channel) MyoII::Dendra2 2 s and 60 s after PC in EC and SOP cells. (B') Lateral side effects of MyoII::Dendra2 following PC. Plot of 561 nm fluorescence intensity of photoconverted channel MyoII::Dendra2 2 s after PC (yellow line). White and black arrows point to photoconverted Dendra2 outside of the photoconverted ROI. (C) PC of Nrv2::Dendra2 finger-like protrusion occurring during SOP cell division. (C') Time lapse illustrating the change in localization of the photoconverted Nrv2::Dendra2 signal. White arrows point toward the lateral spreading of the photoconverted signal at distance of the photoconverted ROI. pIIb and pIIa cells express GAP43::IR under the control of the *neuralized* promoter. Blue dotted circle area represents the non-photoconverted finger-like protrusion. Time is expressed in minutes. (D) Schematic representation of the PC of the midbody of EC. MyoII::Dendra2 is located both at the AJ level and at the midbody level (green). (D') PC of the midbody (lower panel) results in apical MyoII PC (upper panel) localized in the plane of AJs (3 μ m apical to the midbody). All dotted yellow rectangles and discs delineate photoconverted ROIs. Red and blue dots mark the pIIb and pIIa, respectively. Scale bars represent 5 μ m. Time is expressed in seconds (A–D'') and in minutes (C').

μ W) is sufficient to photoconvert the entire cytoplasm of the cell expressing freely diffusing KAEDE in less than 2 s (Figure S2A), these experimental conditions were unsuccessful to photoconvert Notch::mMaple3. For the latter, as experimentally determined by (Trylinski et al. 2017) and confirmed by (Bellec et al. 2021), efficient PC of Notch::mMaple3 is achieved by increasing the number of iterations to 40 within a 2- μ m² rectangular ROI. Because Notch is a transmembrane protein, in contrast to KAEDE that diffuses within microsecond timescale, the signal remains

restricted to the ROI within the next 2 s (time required to carry out the 40 iterations) following PC process (Figure S2B).

However, as the properties of KAEDE and mMaple3 are different, in order to assess the effect of the diffusion rate of the proteins of interest, we next compared probes fused to the same photoconvertible probe and located in the same subcellular domain. We chose SJ components, to avoid a possible difference in laser penetration and diffraction depending on the location of the

probe within the cell (surface or depth). We used Dlg1::Dendra2 and Nrv2::Dendra2, a cytosolic and a transmembrane protein with different $t_{1/2}$ and mobile fraction (Table 1). For both proteins of interest, using the same experimental conditions as before (30 iterations at 2% laser power, see Table 1 and Section 2), the same PC efficiency was observed. This latter is measured as the ratio between the 561 nm signal after PC and the 488 nm signal before PC (Figure 2E,E'). We also noticed that the 561 nm channel photoconverted intensity depends on the initial 488 nm signal (Figure 2E) and on the capacity of 488 nm signal to be diminished after PC (Figure S2D). We also observed that photoconverted Nrv2::Dendra2 signal remained located within the ROI 2 s after PC with a limited spreading outside the photoconverted ROI (Figure 2A,B; black arrows, Figure 2E''). Conversely, the photoconverted Dlg1::Dendra2 rapidly diffused away from the ROI along the SJ (Figure 2C,D; black arrows, Figure 2E''). Similar observations were made after photoconverting the junctional MyoII::Dendra2 (Figure S2C). These results illustrated in Figure 2F–F'' highlight the need to find a compromise between the mobility of the protein and the temporal resolution of image acquisition. This would in turn enable to accurately track the photoconverted fluorescent protein across time and space (Figure 2F'). To overcome this limitation, we next determined the impact that the laser power beam and the number of iterations had on PC efficiency and lateral diffusion.

3.4 | Impact of the UV Laser Beam Power and the Number of Iterations on the Spatial Restrictions of PC

We then investigated the effect of the power of the 405 nm laser beam and the number of iterations on the efficiency of PC of MyoII::Dendra2 (Figure 3). As described above when photoconverting SJ components, we first noticed that the efficiency of PC depends on the initial 488 nm signal (Figure S2A,B). Furthermore, it also depends on the capacity of 488 nm signal to be diminished (Figure S2A',B'), regardless of the laser power and the number of iterations of the UV-405 nm laser. We evaluated the effect of progressively increasing the power of the excitation laser while keeping constant both the number of iterations and the size of the ROI. We increased the laser power from 2% to 10% (corresponding to 4 to 20 μ W laser power at 63X lens exit) in the microscopy Zen Black software (see Section 2). At 2% laser power, the photoconverted area remains restricted to initial ROI and did not spread to the adjacent medial network within the next 2 s (Figure 3A,A', upper panels, Figure S2A,A', black dots). At 5% laser power, the PC efficiency within the ROI is higher than at 2% (Figure 3A,A', middle panels, Figure S2A,A', green dots), as expected but the photoconverted MyoII::Dendra2 is slightly detected outside of the ROI up to a distance of 5 μ m (Figure 3A,A', middle panels, Figure 3E'). At 10% laser power, although the efficiency of PC within the ROI is not significantly improved, the photoconverted MyoII::Dendra2 is detected on the entire medial and junctional MyoII meshwork within 2 s (Figure 3A–A'', lower panels, Figure 3E', Figure S2A,A', orange dots). These data indicate that, while it is necessary to reach a laser power threshold to induce PC, increasing the laser power is not the most effective solution to increase PC efficiency.

As described in the previous paragraph, the number of iterations required to induce efficient PC depends on the characteristics of the photoconvertible protein. Thus, we next investigated the impact of the number of iterations of the laser pulse. We used MyoII::Dendra2 fluorescent photoconvertible protein, which presents lateral diffusion side effects (Figure 1B'). Two iterations at 2% laser intensity are sufficient to photoconvert MyoII::Dendra2 within a 2- μ m diameter disc ROI, which comprises the medial MyoII network (Figure 3C,D; upper panels). The photoconverted protein remained restricted to the ROI, albeit the signal intensity was relatively low. Interestingly, increasing the number of iterations led to an increase in photoconverted signals. This signal remained largely restricted to the ROI, and only a small fraction of the photoconverted signal spread toward the cell periphery (Figure 3C',D', middle panels, Figure 3F,F', Figure S3B–B'). Increasing the number of iterations to 30, resulted in an increase of the photoconverted signal and resulted in a global PC of the MyoII network, inside and outside of the photoconverted ROI (Figure 3C'',D'', lower panels, Figure 3F,F', Figure S3B–B'). Moreover, the combination of 30 iterations with a high laser power (10%) led to the photobleaching of MyoII::Dendra2 detected at 561 nm (photoconverted MyoII::Dendra2) within the ROI, together with efficient PC outside the ROI (Figure S3C,D). Thus, these results indicate that it is preferable to vary the number of iterations rather than the laser power to increase the efficiency of PC. The drawback is that the duration of the PC is proportional to the number of iterations (Figure S3E). Together, these results indicate that for a given photoconvertible fluorescent protein, the experimenter must determine the appropriate laser power and number of iterations in order to optimize the PC efficiency.

3.5 | Photo-Enhancement, Photobleaching Versus PC of Photoconvertible Probes

As described above for MyoII::Dendra2, the excessive laser power and number of iterations leads to photobleaching within the ROI and PC outside the ROI (Figure S3A,A'). Another limitation resides in the ability of Dendra2 and KAEDE, but not mMaple3, to be photoconverted from green to red upon prolonged illumination at 488 nm (Chudakov et al. 2007). One possible explanation lies in the fact that Dendra2 and KAEDE, unlike mMaple3, can be photoconverted at 488 nm with low efficiency (orange plot; Figure S4A).

Indeed, while Dendra2 PC is optimal at 405 nm, time-lapse imaging of MyoII::Dendra2 at 488 nm is sufficient to trigger green to red PC in the entire field of observation (Figure 4A). If the sample has been already imaged using 488 nm, the probe may already be photoconverted (Chudakov et al. 2007). In that case, we recommend photobleaching the signal at 561 nm before any PC experiment. We also investigated the effect of 405 nm excitation (30 iterations at 2% laser power) on the 488 nm wavelength emission signal. Although 405 nm PC induces loss of the 488 nm signal within the photoconverted ROI as the result of effective green to red PC, we also noticed an increase of green signal (488 nm) outside the photoconverted ROI (Figure 4B,B'). This increased 488 nm signal seems to be independent of the photoconvertible probe and occurred both for Dendra2 and mMaple3 (Figure S4B). This effect seems to be independent

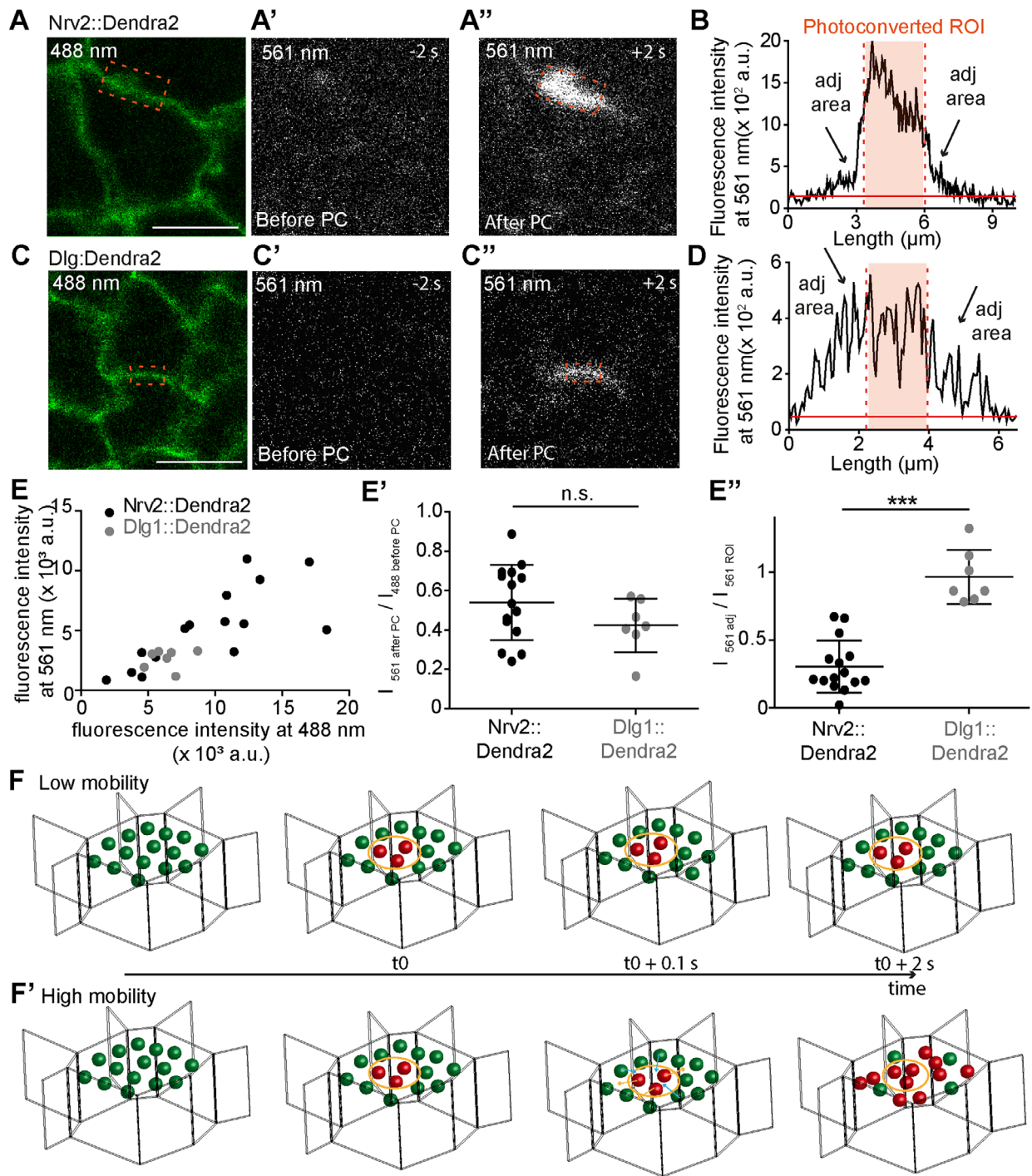


FIGURE 2 | Impact of probe mobility on the monitoring of photoconverted probe. (A–A'', C–C'') localization of Nrv2::Dendra2 (A–A'') and Dlg::Dendra2 in ECs after excitation at 488 nm (A, C), and 561 nm prior to (A', C') or 2 s after 405 nm PC (A'', C''). Dotted red rectangles (A'', A'', C'', C'') indicate the photoconverted ROIs. (B, D) Plot of fluorescence intensity profile for (B) Nrv2::dendra2, (D) Dlg::Dendra2 after PC along the bicellular junction. Black arrows point to the lateral spreading of the photoconverted probe adjacent to the ROI. (E–E'') Efficiency and spreading quantification of Nrv2::Dendra2 and Dlg1::Dendra2 PC assays. (E) Plot of photoconverted 561 nm fluorescence intensity after 405 nm PC in function of initial 488 nm fluorescence intensity ($N = 15$ for Nrv2::Dendra2 and $N = 7$ for Dlg1::Dendra2). (E') Nrv2::Dendra2 (black dots) and Dlg1::Dendra2 (grey dots) quantification of the ratio between the 561 nm photoconverted intensity and the 488 nm initial intensity. (E'') Quantification of the spreading of photoconverted Nrv2::dendra2 and Dlg1::Dendra2 signal outside the photoconverted area. n.s., not statistically significant and *** p value ≤ 0.001 . (F, F') Schematic representation of the sequence of events and spatial side effects for probes with low (E) or high mobility (E'). (F) Probes with low mobility are restricted to the photoconverted area ROI whereas (F') probes with high mobility spread outside photoconverted ROI. If the photoconvertible fluorescent protein is highly mobile, the time required to perform the PC combining with the time required to acquire the first post PC image is too long and does not allow for a complete spatiotemporal tracking post conversion. Green dots represent initial probes before PC. Red dots represent photoconverted probes. Scale bars represent 5 μ m. Dotted orange rectangles represent the photoconverted ROIs. Adj area represents the bi-cellular junction region adjacent to the photoconverted bi-cellular junction ROI. Time is expressed in seconds.

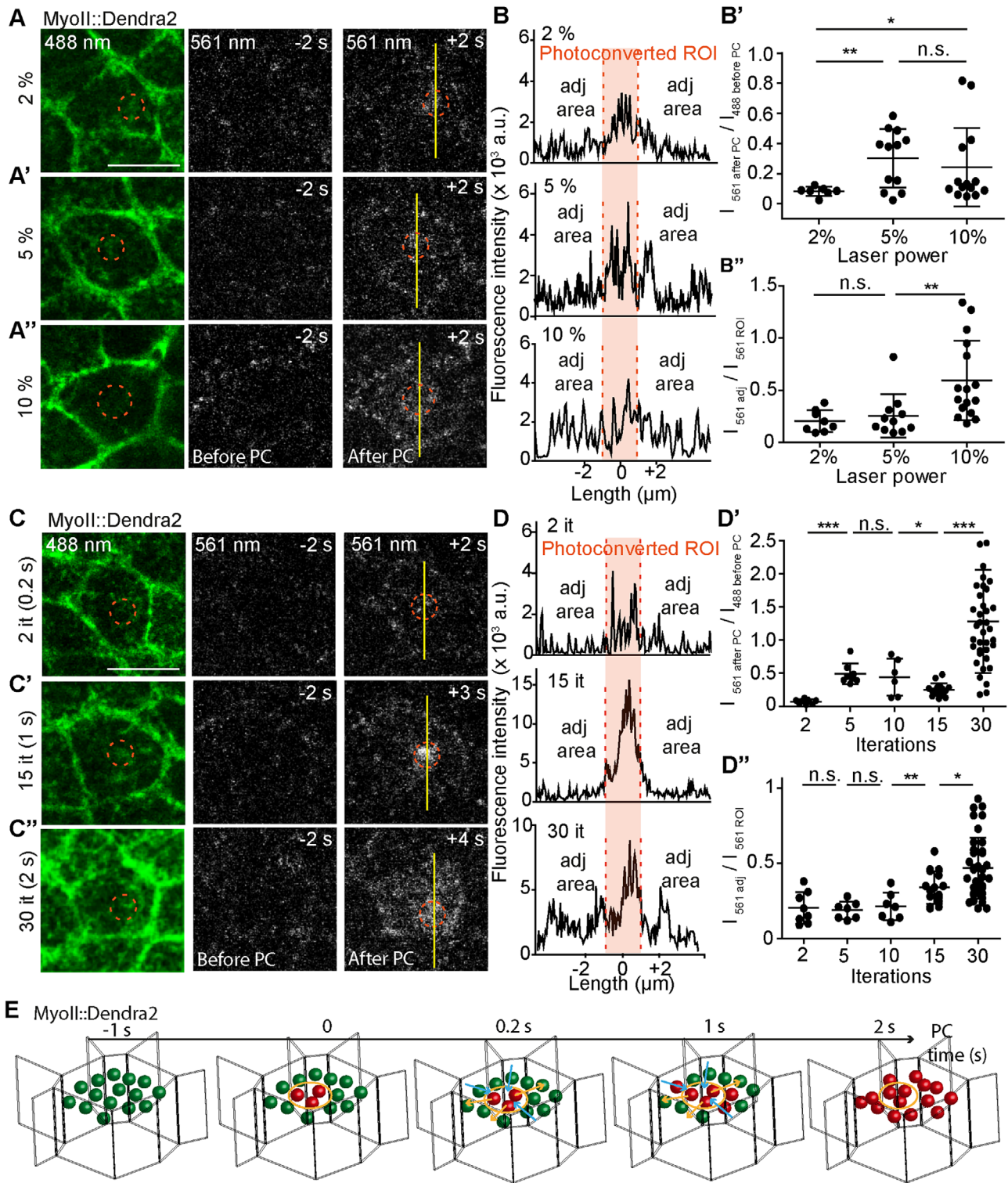


FIGURE 3 | Effect of the laser power and number of iterations on the efficiency of PC of MyoII::Dendra2. (A,A'',C,C'') localization of junctional and medial MyoII::Dendra2 in ECs after excitation at 488 nm (A,C) and at 561 nm prior to (A',C') or after 405 nm PC of a $1\mu\text{m}^2$ ROI depicted by orange dotted circles at 405 nm (A'',C''). In (A), the laser power was increased from 2% to 10% with two iterations, while in (C) the laser power was set to 2% and the number of iterations was increased from 2 to 30. In (C), the time indicated in brackets corresponds to the time needed to make the corresponding number of iterations. (B,D) Plot of fluorescence intensities of the photoconverted MyoII::Dendra2 along the yellow line depicted in A'',C''. The areas highlighted in orange corresponds to the photonconverted ROIs. (B',B'',D',D'') Quantification of the efficiency and spreading of medial MyoII::Dendra2 network following PC. (B') Quantification of the ratio between the 561 nm photoconverted intensity and the 488 nm initial intensity after the PC of MyoII::Dendra2 in a circular ROI using two iterations with 2% ($N = 9$), 5% ($N = 11$), or 10% ($N = 17$) UV laser power at 405 nm. (B'') Quantification of spreading of the MyoII::Dendra2 photoconverted signal at 561 nm adjacent to the photoconverted ROI after the PC of a circular ROI using 2 iterations and 2%, 5%, or 10% UV laser power at 405 nm. (D') Quantification of ratio between the 561 nm photoconverted intensity and the 488 nm initial intensity after the PC of MyoII::Dendra2 in a circular ROI using 2% laser power with 2 ($N = 9$), 5 ($N = 6$), 10 ($N = 6$), 15 ($N = 16$), or 30 iterations ($N = 28$). (D'') Quantification

of the spreading of the MyoII:Dendra2 photoconverted signal adjacent to the photoconverted ROI after the PC of a circular ROI using 2% laser power and 2, 5, 10, 15, or 30 iterations ($N = 28$). n.s., not statistically significant, * p -value ≤ 0.1 and ** p -value ≤ 0.01 . (G) Schematic representation of sequence of events taking place upon increasing the number of 405 nm laser iteration on MyoII::Dendra2. Green and red spheres represent non-photoconverted and photoconverted MyoII::Dendra2, respectively. Orange and blue arrows represent respectively MyoII::Dendra2 that leave or enter within the ROI of PC, respectively. Within 2 s, photoconverted MyoII::Dendra2 occupies the apical surface of the photoconverted cell. Scale bars represent 5 μm . Dotted orange circles represent the photoconverted ROIs. Adj area represents the medial MyoII network region adjacent to the photoconverted myoII network ROI. Time is expressed in seconds.

on the microscope setup as it was observed with a scanning confocal as well as with a spinning disk confocal microscope, while photoconverting MyoII:Dendra2 in larval neural stem cells (Figure S2D–D') (Roubinet et al. 2017). Although we have no solution to propose for overcoming the signal increase in the 488 nm range, the experimenter must be aware of it when quantifying the 488 nm signal after PC.

3.6 | Axial Accuracy of PC

As epithelial cells can be squamous, cuboidal or columnar, organized in single layer, pseudo-stratified or stratified tissues, it is informative to proceed to photomanipulations in 3D. Photoconverting MyoII:Dendra2 in the midbody results in an undesired PC of the MyoII:Dendra2 3 μm apical to the midbody, and over

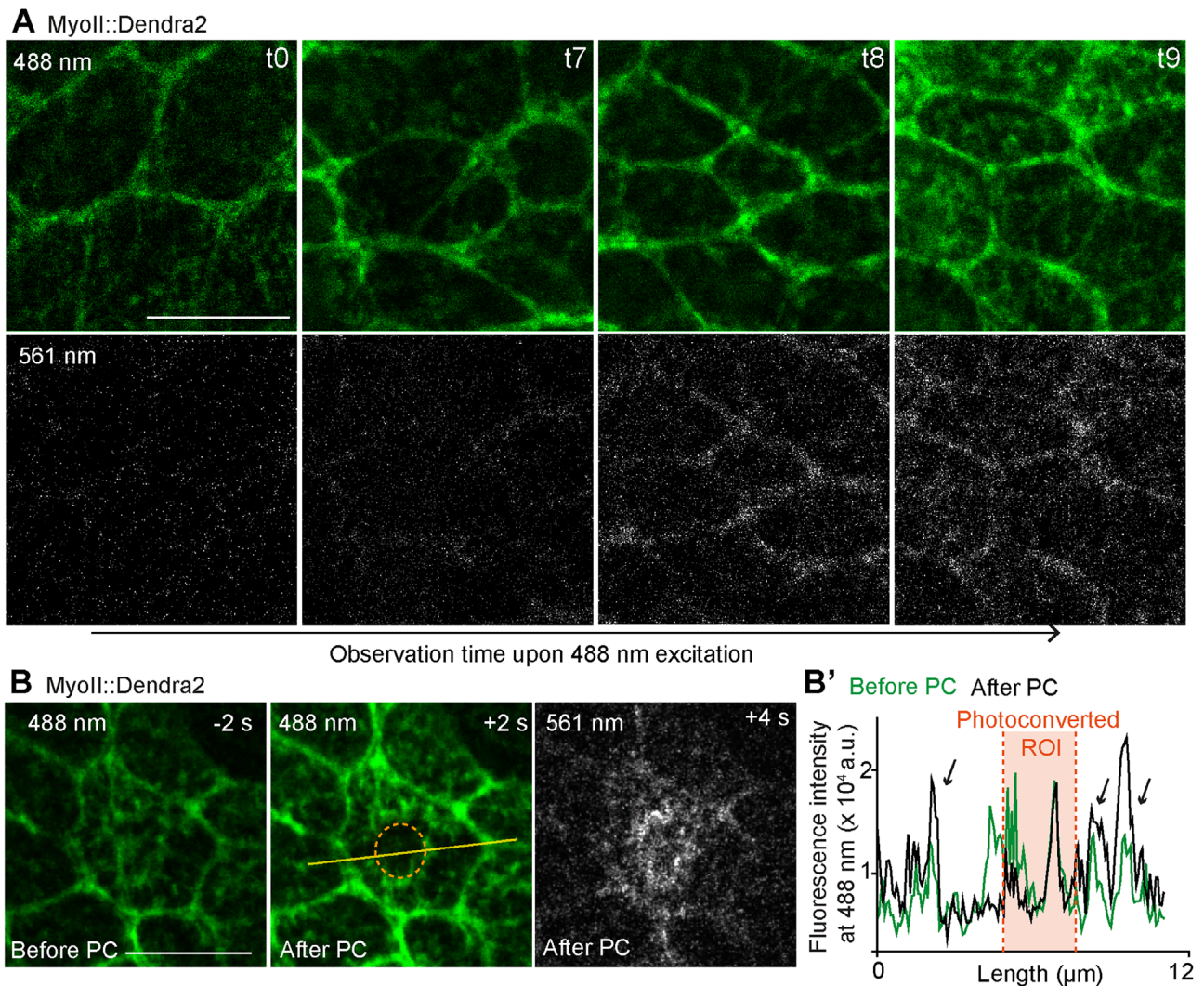


FIGURE 4 | Effect of prolonged illumination of Dendra2 upon excitation at 488 nm and enhancement of green signal upon excitation at 405 nm. (A,A') Imaging of MyoII ::Dendra2 after excitation at 488 nm (A) leads to green to red PC (A'). Time is expressed in minutes after the start of the experiment. (B,B') PC of MyoII::Dendra2 in a 1 μm^2 ROI (orange dotted disc) at 405 nm resulted in a green to red PC detectable upon excitation at 561 nm (B"). The laser power was set to 2% with 30 iterations. While the 405 nm illumination in the ROI causes a reduction of the green signal in the ROI as a result of green to red PC, a general increase in the green signal outside the ROI is observed -upon excitation at 488 nm (B). (B') Plot of 488 nm fluorescence intensity along the yellow line depicted in (B) before (green curve) and after (black curve) PC. Black arrows represent the increase in the 488 nm increase signal upon 405 nm PC. Scale bars represent 5 μm .

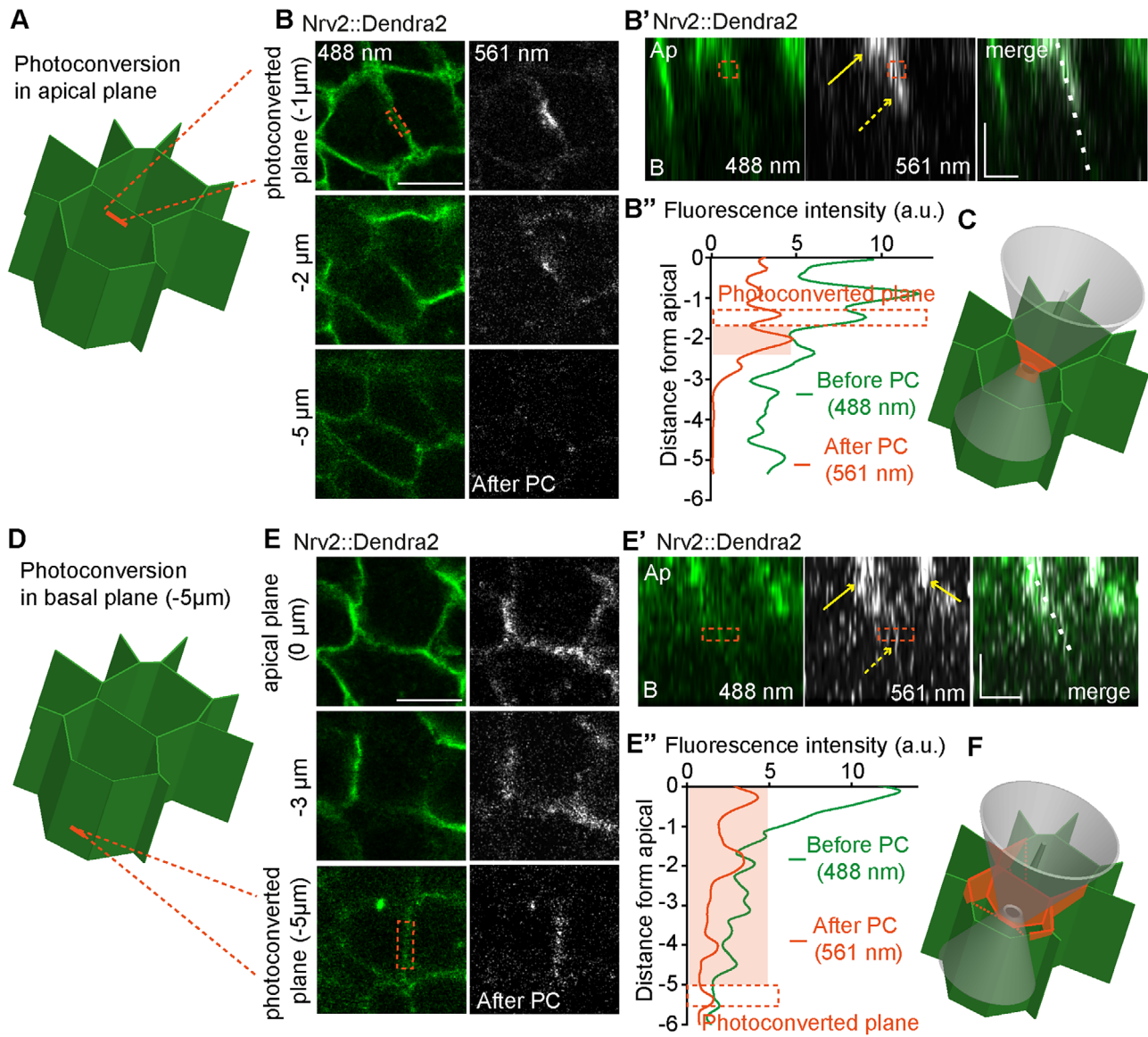


FIGURE 5 | Applications and limitations of PC along the apicobasal axis. (A) Schematic illustration of apical PC of part of the bicellular junction represented by the orange bar. (B) Top view of Nrv2::Dendra2 (green) at -1 , -2 , and -5 μm relative to the apical part of the SJ domain following PC of the ROI depicted in orange at 405 nm. Panels in grey correspond to the photoconverted signal. (B') Orthogonal view of images shown in (B) upon 405 nm PC and passing through the orange photoconverted ROI (B'). Yellow arrows indicate the respective apical and lateral spreading of the PC. (B'') Apicobasal plot profile of the fluorescence signal prior to (green line, signal at 488 nm excitation) or following 405 nm PC (black line, signal at 561 nm excitation). Photoconverted area is depicted in orange dashed line, plain orange rectangle represents the 1 μm lateral spreading below the photoconverted ROI. (C) Schematic representation of PC double light cone (grey) and low incidence of apical PC on Nrv2::Dendra2 located in basal planes (orange area) ($N = 4$). (D) Schematic representation of PC of a ROI depicted by an orange line and located at the basal rim of the bicellular junction. Orange bar represents PC ROI. (E) Top view of Nrv2::Dendra2 (green) at 0, -3 , and -5 μm relative to the apical part of the SJ domain following PC of the ROI depicted in orange at 405 nm. Panels in grey correspond to the photoconverted signal. (E') orthogonal view of the images shown in (E) and passing through the ROI depicted in orange dashed lines. Solid and dotted yellow arrows indicate the respective apical and lateral axial spreading of the PC. (E'') Apicobasal plot profile of the fluorescence signal prior to (green line, signal at 488 nm excitation) or following PC (black line, signal at 561 nm excitation). Photoconverted area is depicted in orange dashed line, plain orange rectangle represents the 4 μm apical spreading above the photoconverted ROI ($n = 9$). (F) Schematic representation of the double light cone of PC illumination (grey) illustrating the consequences of basal PC (orange) on apical planes (orange area). Scale bars represent 5 μm .

an area of 5 μm in diameter (Figure 1C'). To better describe the secondary effects of PC along the apicobasal depth axis, we photoconverted apical or basolateral ROIs and measured the respective lateral and axial distribution of the photoconverted signal (Figure 5A,D). To this aim, Nrv2::Dendra2 was chosen as

SJs span over a height of 4 to 5.5 μm (Esmangart de Bournonville & Le Borgne, 2020); (Daniel et al. 2018). The PC protocol was set at 2% laser beam power and 30 iterations, to ensure effective PC within the ROI while limiting lateral spreading (Figure 2A''–E''). When photoconverted apically (orange rectan-

gle, Figure 5B, upper panel), the Nrv2::Dendra2 photoconverted signal is detected within the ROI in the confocal plane of the ROI. However, due to the axial effect of the laser beam forming a double cone of light, PC is not confined to the plane of the ROI, but also occurs in the apical and basal planes of the targeted area covering an area of 3 μm thick in this example (Figure 5B–B’). This axial effect is even more noticeable when the PC is performed deeper at 5.5 μm below the apical surface (Figure 5D–E’). Indeed, as the laser beam is going through the focal planes located apical to the ROI, effective PC of Nrv2::Dendra2 occurs along the apicobasal axis. In this case, the apical surface area on which photoconverted probes is detected following PC of a basally located ROI is much broader than the ROI, spreading over a diameter of about 10 μm , that is, the diameter of the cone of light in this particular apical plane (Figure 5E), upper panel; Figure S5A; large field of apical view). Similar results were obtained upon basal PC of Notch::mMaple3 (Bellec et al. 2021). This indicates that the effect is not dependent on the photoconvertible protein, but is instead caused by the cone of light. This cone of light is the main limitation for PC experiments. One way to overcome this problem was proposed by (Trylinski et al. 2017). If the sample allows it, it would suffice to rotate specimen to visualize the cells of interest from the lateral side instead of the top view. Another alternative is to use a two-photon laser beam to prevent the axial effect of the conventional laser beam as done in mitochondria tracking (Ivanchenko et al. 2007; Watanabe et al., 2007) or in cell tracking (Chtanova et al. 2014). It has been reported that two-photon mediated PC of KAEDE requires hundreds of iterations cycles at 810 nm (Chtanova et al. 2014). In line with this study, we observed that while increasing laser power in combination with 100 iterations is not sufficient to induce PC (Figure S5B), the PC of cytosolic KAEDE occurred from 500 iterations onward combined with 0.5% of 810 nm laser power. The 561 nm channel photoconverted intensity, corresponding to the efficiency of the PC, progressively increases with the number of iterations from 500 to 1200 (Figure S5B’). However, in these conditions, the KAEDE PC is around five to six times less efficient than that obtained by two iterations with a one-photon laser (Figure S5B’). To quantify and compare the PC efficiency between UV 405 nm and two-photon IR-810 nm, we performed PC of Nrv2::Dendra2 with 1500 iterations protocol (Figure S5C–C’). As for KAEDE experiments, we observed that the IR-810 nm Nrv2::Dendra2 PC efficiency is 10 times lower than that obtained with one-photon UV 405 nm (Figure S5D–D’). A second limitation to the use of a two-photon laser is the time required for PC. This ranges from around 1 (500 iterations) to 3 min (1500 iterations), compared to the 2s (40 iterations) time required for PC with one-photon laser. Next, we studied the extent to which the use of two-photon lasers avoids the effects of axial PC inherent in one-photon laser. To do so, we performed two-photon PC at 810 nm of a Nrv2::Dendra2 bicellular junction and a z-stack was acquired. Despite the lower efficiency observed (Figure S5D’), and in striking contrast to 405 nm PC, the PC at 810 nm remains restricted to the PC plane (around $-4 \mu\text{m}$ to the apical plane of the cell). In this case, there is almost no drooling along the apicobasal axis (1 μm) (Figure S5E’, S5E’), compared to the massive apical PC that follows PC with the 405 nm wavelength (Figure S5E and Figure 5D). These results demonstrate that although the two-photon laser PC approach is relevant for circumventing axial artifacts, the signals detected remain weak. As a result, this decreases the signal-to-noise ratio and makes quantification more delicate. In addition,

the time required for PC in this setup is unsuitable for probes with high mobilities.

3.7 | Conclusion

This study provides a framework to help designing and carrying out PC experiments on epithelial cells using confocal microscopes present on most imaging facilities. Our results clearly demonstrate the value of the approach, while underlining that the PC protocol is “not a plug and play” one to perform qualitative and quantitative studies. Hence, by using various proteins of interest with different degrees of mobility, we highlighted the lateral and axial artifacts observable during PC experiments *in vivo*. We also proposed means to bypass these side effects (Table 1).

We have demonstrated here that Dendra2 PC of subcellular population of tagged protein expressed at physiological levels within epithelium is easily achievable, but can induce undesired spatial effects such as lateral and axial spreading outside the photoconverted ROI. We presented on Figures 2 and 3 that the spreading depends on the mobility of the photoconvertible probes and the experimental parameters namely laser power and number of iterations. Given that the optimal parameters have to be defined empirically, we concluded, that in order to increase the PC efficiency it is preferable to modify the number of iterations rather than the laser power. The main question at the start of a PC experiment is how to define the first set of experimental parameters. To help the experimenter, we report here the data from minute time-scale FRAP experiments (mobile fraction and half time $t_{1/2}$ recovery parameters; Figure S6). We also include data from PC experiments (laser power and number of iterations) for the different cytosolic and transmembrane fluorescent photoconvertible proteins used in this study in Table 1. For fluorescent associated probes having a small mobile fraction such as Nrv2 and Notch (0.19 for ATPalpha::YFP (Oshima and Fehon 2011) and 0.31 for Notch::GFP), the efficient PC is obtained with a low laser power and a high number of iterations (Table 1). In contrast, for GFP fluorescent proteins having a high mobility, such as MyoII, Dlg1, or KAEDE, it is preferable to increase the laser power and reduce the number of iterations. In doing so, the photoconverted signal remains restricted as much as possible to the photoconverted ROI. From the results summarized in Table 1, before initiating an experiment, we propose to perform FRAP measurements analysis. Depending on the FRAP recovery parameters obtained (Table 1, Figure S6), we propose starting PC with low laser power and a modulation of the number of iterations (Table 1), with respectively a low number of iterations (between 2 and 5) for GFP-associated probes that present high mobile fraction (above 0.8) in FRAP recovery analysis, and a high number of iterations (higher than 20) for probes that present low mobile fraction. Depending on the fluorescent photoconvertible protein localization, we also report the benefits and limitations of the one photon 405 nm PC compared to the two-photon PC (10th column; SJ components).

4 | Discussion

In this study, we have characterized the side effects upon PC on living *Drosophila* pupae and their impacts and biases to post-

PC analyses. We focused mainly on Dendra2 photoconvertible fluorescent probes that were expressed in different subcellular locations such as the Myosin II contractile network and SJ components. We report that 405 nm UV photoconversion leads to two-dimensional spreading effects that depend primarily on the mobility of the photoconvertible probe. Although these subcellular spatial side effects were previously observed (Sattarzadeh et al. 2015), their spatiotemporal description on the second time scale after PC and on global post PC analysis were missing. We also report the axial spreading along the basolateral axis depending on the nature of UV 405 nm PC assay. Based on these considerations and our in vivo results in the notum of *D. melanogaster*, we summarize the different biases that appear upon PC, and indicate possible strategies to minimize them (Table 1).

Previous ex vivo and in vivo analyses recapitulate the optical properties of excitation and emission of the different photoconvertible proteins used in this study (Lombardo et al. 2012; Day and Davidson 2009). Knowing the folding and diffusion rates of the protein of interest is an important prerequisite for selecting the experimental setup and the photoconvertible probe. The importance of knowing the diffusion rate is illustrated by cytosoluble KAEDE. In this case, a single UV pulse in a limited volume results in the PC of the entire volume of the cell in the space within less than 2 s. If one wishes to study the diffusion rate of a highly mobile protein, the imaging speed becomes a limiting factor. This demands a highly sensitive microscope capable of producing images within tens of milliseconds, such as a spinning disk confocal microscope (Woods et al. 2014). As for the importance of the kinetics of protein folding, we report that the level of fluorescent signal varies among the photoconvertible tags (Notch::Dendra2 vs. Notch::mMaple3; Figure S1B–B"). As shown for the Notch receptor, while the distribution of Notch::mMaple3 is similar to that of Notch::GFP, in contrast, while being functional, Notch::Dendra2 is almost not detected at the plasma membrane. In such a case, the use of faster folding probes such as mMaple3 is recommended (Trylinski et al. 2017; Bellec et al. 2021). It is important to note that all the experiments were carried out at 25°C, and to bear in mind that the rate at which the probes fold will depend on the model system, the rearing and imaging temperature.

Once the choice of photoconvertible fluorescent probe has been made, we report that the PC efficiency depends on the excitation power and the PC time at 405 nm, defined by the number of iterations. We report that the laser power excitation impacted directly on PC efficiency and noticed how a significant increase in the 405 nm UV power during PC promotes spreading of the photoconverted probe outside the defined photoconverted ROI (Figure 3). This also results in the photobleaching of the desired photoconverted ROI (Figure S3). Similar phenomenon has been described in (Wulflele et al. 2022). In that case, the PC efficiency of mEos4b strongly depended on the applied-405 nm PC illumination conditions. In particular, it has been shown that high 405 nm intensity decrease the efficiency of mEos4b PC due to non-linear bleaching of the 488 nm green state. The increase of the PC time is thus preferable in PC assays to limit the spreading effects outside the photoconverted ROI (Figure 3). However, increasing the duration of PC (1 to

3 s in our sets of experiments; Figure 3), became rate limiting for proteins with high mobility rate such as Myo-II. Thus, the combination of PC parameters namely laser power relative to the number of iterations needs to be adjusted for each protein of interest.

In this study, Dendra2 probe was mainly used as it presents bright fluorescence in both initial and photoactivated state, and low phototoxic activation with the 488 nm (Baker et al. 2010; McKinney et al. 2009; Chudakov et al. 2007). Thanks to these features, it is well adapted for the tracking of super resolution images. However, Dendra2 presents some potential disadvantages such as low PC, and a 561 nm photoconverted stage prone to photobleaching (Chudakov et al. 2007). Furthermore, the Dendra2 displays a second efficient PC peak around 490 nm (McKinney et al. 2009; Gurskaya et al. 2006) that sensitize Dendra2 to 488 nm light and allows its PC upon 488 nm excitation (Figure 4A and Chudakov et al. 2007). As proposed by (Baker et al. 2010), illumination can be attenuated by a neutral density filter, or as shown in our study by a low 488 nm excitation laser power. Alternatively, when using a scanning confocal microscope in order to limit the analysis bias due to the 488 nm PC, we recommend to perform photobleaching of 561 nm channel before UV 405 nm PC. This will enable the separation of UV 405 nm PC from the level at 488 nm PC due to imaging.

As we report here, the most annoying effect of using a UV laser for PC is the undesired axial photo conversion. This turns out to be not too limiting while using thin specimens (cell cultures) or photoconverting probes located in the confocal plane close to the coverslip (apical plane of epithelial cells for example). However, the PC in basal planes systematically results in concomitant apical PC. It makes interpretation and lateral quantification complicated. Interestingly, previous studies on HeLa cells overexpressing photoactivable-GFP that (Schneider et al. 2005) show that photoactivation can be done in the spectral region ranging from 720 to 840 nm. This results in a sharper and more controllable three-dimensional activation volume than with a 405 nm illumination. Applying this strategy to photoconvertible fluorescent proteins could offer a wide variety of potential applications such as subcellular three-dimensional PC. Previous studies on HEK293 cells expressing the cytokeratin 18-d2EosFP photoconvertible probe show an improvement of 2D spatial resolution with two-photon excitation at 808 nm (Wiedenmann et al. 2004). Additionally, PC, in HeLa cells, of EosFP-tagged mitochondria at 970 nm was successful three-dimensionally using two-photon conversion (Ivanchenko et al. 2007). Based on Chtanova et al. (2014) protocol that used hundreds of cycles to photoconvert KAEDE in mice cells, we successfully photoconverted cytosoluble KAEDE and transmembrane Nrv2::Dendra2. We used a 810 nm two-photon through and an increase in the number of PC iterations from 500 to 1500 compared with the 40 iterations used for 405 nm one-photon PC. Whereas two-photon PC induces a drastic reduction of the light cone (Figure S5D), 810 nm two-photon PC is 10 times less efficient than 405 nm UV PC (Figures S5B and S5C). In addition, the time required to photoconvert 2 μm^2 ROI upon 810 nm two-photon may be a limiting factor when studying proteins with seconds time scale mobility. Thus, we conclude that 810 nm two-photon PC may be limited to slow diffusing proteins expressed at high levels.

Author Contributions

Conceptualization: Roland Le Borgne and Mathieu Pinot. **Methodology:** Mathieu Pinot, Céline Bruelle (KAEDE experiments), Marie André, Chantal Roubinet (neural stem cells experiments) Roland Le Borgne. **Validation:** Mathieu Pinot, Roland Le Borgne. **Formal analysis:** Mathieu Pinot. **Investigation:** Mathieu Pinot, Marie André. **Writing – original draft:** Mathieu Pinot, Roland Le Borgne. **Visualization:** Mathieu Pinot, Céline Bruelle, Marie André, Chantal Roubinet, Roland Le Borgne. **Supervision:** Roland Le Borgne, Mathieu Pinot. **Project administration:** Roland Le Borgne.

Acknowledgments

We thank F. Schweisguth, C. Klambt, the Bloomington Drosophila Stock Center, the Vienna Drosophila Resource Center and InDroso for providing fly stocks. We thank L. Chesneau, J. Kubiak, M. Mira Osuna and E. George for critical reading. We thank S. Dutertre, X. Pinson and G. Le Marchand of the Microscopy Rennes Imaging Center (MRic, BIOSIT, Biogenouest) for assistance. MRic is member of the national infrastructure France-BioImaging supported by the French National Research Agency (ANR-10-INBS-04). Funding acquisition: R.L.B (ANR-20-CE13-0015), M.P. (Université de Rennes, AAP défis émergents 2021).

Conflicts of Interest

The authors declare no conflicts of interest.

References

- Ando, R., Hama H., Yamamoto-Hino, M., Mizuno, H., and A. Miyawaki. 2002. “An Optical Marker Based on the UV-induced Green-to-Red Photoconversion of a Fluorescent Protein.” *Proceedings of the National Academy of Sciences* 99, no. 20: 12651–12656, <https://doi.org/10.1073/pnas.202320599>.
- Baker, S. M., R. W. Buckheit 3rd, and M. M. Falk. 2010. “Green-to-Red Photoconvertible Fluorescent Proteins: Tracking Cell and Protein Dynamics on Standard Wide-Field Mercury Arc-Based Microscopes.” *BMC Cell Biology [Electronic Resource]* 11: 15, <https://doi.org/10.1186/1471-2121-11-15>.
- Bakshi, S., B. P. Bratton, and J. C. Weisshaar. 2011. “Subdiffraction-Limit Study of Kaede Diffusion and Spatial Distribution in Live *Escherichia coli*.” *Biophysical Journal* 101, no. 10: 2535–2544, <https://doi.org/10.1016/j.bpj.2011.10.013>.
- Bellec, K., I. Gicquel, and R. Le Borgne. 2018. “Stratum Recruits Rab8 at Golgi Exit Sites to Regulate the Basolateral Sorting of Notch and Sanpodo.” *Development (Cambridge, England)* 145, no. 13: dev163469, <https://doi.org/10.1242/dev.163469>.
- Bellec, K., M. Pinot, I. Gicquel, and R. Le Borgne. 2021. “The Clathrin Adaptor AP-1 and Stratum Act in Parallel Pathways to Control Notch Activation in Drosophila Sensory Organ Precursor Cells.” *Development (Cambridge, England)* 148, no. 1: dev191437, <https://doi.org/10.1242/dev.191437>.
- Bruelle, C., M. Pinot, E. Daniel, M. Daudé, J. Mathieu, and R. Le Borgne. 2023. “Cell-Intrinsic and -Extrinsic Roles of the ESCRT-III Subunit Shrub in Abscission of Drosophila Sensory Organ Precursors.” *Development (Cambridge, England)* 150, no. 10: dev201409, <https://doi.org/10.1242/dev.201409>.
- Campbell, R. E., O. Tour, A. E. Palmer, et al. 2002. “A Monomeric Red Fluorescent Protein.” *Proceedings of the National Academy of Sciences* 99, no. 12: 7877–7882, <https://doi.org/10.1073/pnas.082243699>.
- Chtanova, T., H. R. Hampton, L. A. Waterhouse, et al. 2014. “Real-Time Interactive Two-photon Photoconversion of Recirculating Lymphocytes for Discontinuous Cell Tracking in Live Adult Mice.” *Journal of Biophotonics* 7, no. 6: 425–433, <https://doi.org/10.1002/jbpo.201200175>.
- Chudakov, D. M., S. Lukyanov, and K. A. Lukyanov. 2007. “Using Photoactivatable Fluorescent Protein Dendra2 to Track Protein Movement.” *Biotechniques* 42, no. 5: 553, 555, 557 passim, <https://doi.org/10.2144/000112470>.
- Couturier, L., K. Mazouni, and F. Schweisguth. 2013. “Numb Localizes at Endosomes and Controls the Endosomal Sorting of Notch After Asymmetric Division in Drosophila.” *Current Biology* 23, no. 7: 588–593, <https://doi.org/10.1016/j.cub.2013.03.002>.
- Daniel, E., M. Daudé, I. Kolotuev, K. Charish, V. Auld, and R. Le Borgne. 2018. “Coordination of Septate Junctions Assembly and Completion of Cytokinesis in Proliferative Epithelial Tissues.” *Current Biology* 28, no. 9: 1380–1391.e1384, <https://doi.org/10.1016/j.cub.2018.03.034>.
- Day, R. N., and M. W. Davidson. 2009. “The Fluorescent Protein Palette: Tools for Cellular Imaging.” *Chemical Society Reviews* 38, no. 10: 2887–2921, <https://doi.org/10.1039/b901966a>.
- Esmangart de Bournonville, T., and R. Le Borgne. 2020. “Interplay between Anakonda, Gliotactin, and M6 for Tricellular Junction Assembly and Anchoring of Septate Junctions in Drosophila Epithelium.” *Current Biology*, 30, no. 21, 4245–4253.e4, <https://doi.org/10.1016/j.cub.2020.07.090>.
- Fang, Z., N. Takizawa, K. A. Wilson, et al. 2010. “The Membrane-Associated Protein, Supravillin, Accelerates F-Actin-Dependent Rapid Integrin Recycling and Cell Motility.” *Traffic (Copenhagen, Denmark)* 11, no. 6: 782–799, <https://doi.org/10.1111/j.1600-0854.2010.01062.x>.
- Gho, M., Y. Bellaïche, and F. Schweisguth. 1999. “Revisiting the Drosophila Microchaete Lineage: A Novel Intrinsically Asymmetric Cell Division Generates a Glial Cell.” *Development (Cambridge, England)* 126, no. 16: 3573–3584, <https://doi.org/10.1242/dev.126.16.3573>.
- Gurskaya, N. G., V. V. Verkhusha, A. S. Shcheglov, et al. 2006. “Engineering of a Monomeric Green-to-Red Photoactivatable Fluorescent Protein Induced by Blue Light.” *Nature Biotechnology* 24, no. 4: 461–465, <https://doi.org/10.1038/nbt1191>.
- Hagedorn, E. J., J. W. Ziel, M. A. Morrissey, et al. 2013. “The Netrin Receptor DCC Focuses Invadopodia-Driven Basement Membrane Transmigration In Vivo.” *Journal of Cell Biology* 201, no. 6: 903–913, <https://doi.org/10.1083/jcb.201301091>.
- Hatta, K., H. Tsujii, and T. Omura. 2006. “Cell Tracking Using a Photoconvertible Fluorescent Protein.” *Nature Protocols* 1, no. 2: 960–967, <https://doi.org/10.1038/nprot.2006.96>.
- Heisenberg, C. P., and Y. Bellaïche. 2013. “Forces in Tissue Morphogenesis and Patterning.” *Cell* 153, no. 5: 948–962, <https://doi.org/10.1016/j.cell.2013.05.008>.
- Houssin, E., M. Pinot, K. Bellec, and R. Le Borgne. 2021. “Par3 cooperates With Sanpodo for the Assembly of Notch Clusters Following Asymmetric Division of Drosophila Sensory Organ Precursor Cells.” *Elife* 10: e66659, <https://doi.org/10.7554/eLife.66659>.
- Ivanchenko, S., S. Glaschick, C. Röcker, F. Oswald, J. Wiedenmann, and G. U. Nienhaus. 2007. “Two-Photon Excitation and Photoconversion of EosFP in Dual-Color 4Pi Confocal Microscopy.” *Biophysical Journal* 92, no. 12: 4451–4457, <https://doi.org/10.1529/biophysj.106.103408>.
- Kang, M., C. A. Day, E. DiBenedetto, and A. K. Kenworthy. 2010. “A Quantitative Approach to Analyze Binding Diffusion Kinetics by Confocal FRAP.” *Biophysical Journal* 99, no. 9: 2737–2747, <https://doi.org/10.1016/j.bpj.2010.09.013>.
- Leduc, C., and S. Etienne-Manneville. 2017. “Regulation of Microtubule-Associated Motors Drives Intermediate Filament Network Polarization.” *Journal of Cell Biology* 216, no. 6: 1689–1703, <https://doi.org/10.1083/jcb.201607045>.
- Lele, T., P. Oh, J. A. Nickerson, and D. E. Ingber. 2004. “An Improved Mathematical Approach for Determination of Molecular Kinetics in Living Cells With FRAP.” *Mechanics & Chemistry of Biosystems: MCB* 1, no. 3: 181–190.
- Lippincott-Schwartz, J., E. Snapp, and A. Kenworthy. 2001. “Studying Protein Dynamics in Living Cells.” *Nature Reviews Molecular Cell Biology* 2, no. 6: 444–456, <https://doi.org/10.1038/35073068>.

- Lippincott-Schwartz, J., E. L. Snapp, and R. D. Phair. 2018. "The Development and Enhancement of FRAP as a Key Tool for Investigating Protein Dynamics." *Biophysical Journal* 115, no. 7: 1146–1155, <https://doi.org/10.1016/j.bpj.2018.08.007>.
- Lombardo, V. A., A. Sporbert, and S. Abdelilah-Seyfried. 2012. "Cell Tracking Using Photoconvertible Proteins During Zebrafish Development." *Journal of Visualized Experiments: JOVE* no. 67: 4350, <https://doi.org/10.3791/4350>.
- Mathur, J., S. Griffiths, K. Barton, and M. H. Schattat. 2012. "Green-to-Red Photoconvertible mEosFP-Aided Live Imaging in Plants." *Methods in Enzymology* 504: 163–181, <https://doi.org/10.1016/b978-0-12-391857-4.00008-2>.
- Mavrikakis, M., R. Rikhy, and J. Lippincott-Schwartz. 2009. "Cells Within a Cell: Insights Into Cellular Architecture and Polarization From the Organization of the Early Fly Embryo." *Communicative and Integrative Biology* 2, no. 4: 313–314, <https://doi.org/10.4161/cib.2.4.8240>.
- McKinney, S. A., C. S. Murphy, K. L. Hazelwood, M. W. Davidson, and L. L. Looger. 2009. "A Bright and Photostable Photoconvertible Fluorescent Protein." *Nature Methods* 6, no. 2: 131–133, <https://doi.org/10.1038/nmeth.1296>.
- Michelman-Ribeiro, A., D. Mazza, T. Rosales, et al. 2009. "Direct Measurement of Association and Dissociation Rates of DNA Binding in Live Cells by Fluorescence Correlation Spectroscopy." *Biophysical Journal* 97, no. 1: 337–346, <https://doi.org/10.1016/j.bpj.2009.04.027>.
- Nowotschin, S., and A. K. Hadjantonakis. 2009. "Use of KikGR a Photoconvertible Green-to-Red Fluorescent Protein for Cell Labeling and Lineage Analysis in ES Cells and Mouse Embryos." *BMC Developmental Biology* 9: 49, <https://doi.org/10.1186/1471-213x-9-49>.
- Oshima, K., and R. G. Fehon. 2011. "Analysis of Protein Dynamics Within the Septate Junction Reveals a Highly Stable Core Protein Complex That Does Not Include the Basolateral Polarity Protein Discs Large." *Journal of Cell Science* 124, no. Pt 16: 2861–2871, <https://doi.org/10.1242/jcs.087700>.
- Pigazzini, M. L., and J. Kirstein. 2020. "In Vivo Quantification of Protein Turnover in Aging *C. elegans* Using Photoconvertible Dendra2." *Journal of Visualized Experiments: JOVE* no. 160: 1–18, <https://doi.org/10.3791/61196>.
- Roubinet, C., A. Tsankova, T. T. Pham, et al. 2017. "Spatio-Temporally Separated Cortical Flows and Spindle Geometry Establish Physical Asymmetry in Fly Neural Stem Cells." *Nature Communications* 8, no. 1: 1383, <https://doi.org/10.1038/s41467-017-01391-w>.
- Rujano, M. A., D. Briand, B. Đelić, J. Marc, and P. Spéder. 2022. "An Interplay Between Cellular Growth and atypical Fusion Defines Morphogenesis of a Modular Glial Niche in *Drosophila*." *Nature Communications* 13, no. 1: 4999, <https://doi.org/10.1038/s41467-022-32685-3>.
- Sattarzadeh, A., R. Saberianfar, W. R. Zipfel, R. Menassa, and M. R. Hanson. 2015. "Green to Red Photoconversion of GFP for Protein Tracking In Vivo." *Scientific Reports* 5: 11771, <https://doi.org/10.1038/srep11771>.
- Schneider, M., S. Barozzi, I. Testa, M. Faretta, and A. Diaspro. 2005. "Two-Photon Activation and Excitation Properties of PA-GFP in the 720–920-nm Region." *Biophysical Journal* 89, no. 2: 1346–1352, <https://doi.org/10.1529/biophysj.104.054502>.
- Schweisguth, F. 2015. "Asymmetric Cell Division in the *Drosophila* Bristle Lineage: From the Polarization of Sensory Organ Precursor Cells to Notch-Mediated Binary Fate Decision." *Wiley Interdisciplinary Reviews. Developmental Biology* 4, no. 3: 299–309, <https://doi.org/10.1002/wdev.175>.
- Tomura, M., N. Yoshida, J. Tanaka, et al. 2008. "Monitoring Cellular Movement in Vivo With Photoconvertible Fluorescence Protein "Kaede" Transgenic Mice." *Proceedings of the National Academy of Sciences* 105, no. 31: 10871–10876, <https://doi.org/10.1073/pnas.0802278105>.
- Trylinski, M., K. Mazouni, and F. Schweisguth. 2017. "Intra-lineage Fate Decisions Involve Activation of Notch Receptors Basal to the Midbody in *Drosophila* Sensory Organ Precursor Cells." *Current Biology* 27, no. 15: 2239–2247.e2233, <https://doi.org/10.1016/j.cub.2017.06.030>.
- Tsien, R. Y. 1998. "The Green Fluorescent Protein." *Annual Review of Biochemistry* 67: 509–544, <https://doi.org/10.1146/annurev.biochem.67.1.509>.
- Wang, J., M. Michel, L. Bialas, G. Pierini, and C. Dahmann. 2023. "Preferential Recruitment and Stabilization of Myosin II at Compartment Boundaries in *Drosophila*." *Journal of Cell Science* 136, no. 5: jcs260447, <https://doi.org/10.1242/jcs.260447>.
- Wang, K., C. Wloka, and E. Bi. 2019. "Non-muscle Myosin-II Is Required for the Generation of a Constriction Site for Subsequent Abscission." *iScience* 13: 69–81, <https://doi.org/10.1016/j.isci.2019.02.010>.
- Watanabe, W., T. Shimada, S. Matsunaga, et al. 2007. "Single-Organella Tracking by Two-Photon Conversion." *Opt Express* 15, no. 5: 2490–2498, <https://doi.org/10.1364/oe.15.002490>.
- Wavreil, F. D. M., J. Poon, G. M. Wessel, and M. Yajima. 2021. "Light-induced, Spatiotemporal Control of Protein in the Developing Embryo of the Sea Urchin." *Developmental Biology* 478: 13–24, <https://doi.org/10.1016/j.ydbio.2021.06.006>.
- Wiedenmann, J., S. Ivanchenko, F. Oswald, et al. 2004. "EosFP, A Fluorescent Marker Protein With UV-inducible Green-to-Red Fluorescence Conversion." *Proceedings of the National Academy of Sciences* 101, no. 45: 15905–15910, <https://doi.org/10.1073/pnas.0403668101>.
- Woods, E., J. Courtney, D. Scholz, W. W. Hall, and V. W. Gautier. 2014. "Tracking Protein Dynamics With Photoconvertible Dendra2 on Spinning Disk Confocal Systems." *Journal of Microscopy* 256, no. 3: 197–207, <https://doi.org/10.1111/jmi.12172>.
- Wulffle, J., D. Thédié, O. Glushonkov, and D. Bourgeois. 2022. "mEos4b Photoconversion Efficiency Depends on Laser Illumination Conditions Used in PALM." *Journal of Physical Chemistry Letters* 13, no. 22: 5075–5080, <https://doi.org/10.1021/acs.jpclett.2c00933>.

Supporting Information

Additional supporting information can be found online in the Supporting Information section.